Concurrent three-dimensional characterization of the refractive-index and residual-stress distributions in optical fibers

Michael R. Hutsel and Thomas K. Gaylord*

School of Electrical and Computer Engineering, Georgia Institute of Technology, 777 Atlantic Drive NW, Atlanta, Georgia 30332-0250, USA

*Corresponding author: tgaylord@ece.gatech.edu

Received 9 April 2012; revised 18 June 2012; accepted 27 June 2012; posted 28 June 2012 (Doc. ID 166288); published 27 July 2012

A three-dimensional index-stress distribution (3DISD) measurement method for determining concurrently the refractive-index distributions (RIDs) and residual-stress distributions (RSDs) in optical fibers is presented. The method combines the quantitative-phase microscopy technique, the Brace–Köhler compensator technique, and computed tomography principles. These techniques are implemented on a common apparatus to enable concurrent characterization of the RID and the RSD. Measurements are performed on Corning SMF-28 fiber in an unperturbed section and in a section exposed to CO_2 laser radiation. The concurrent measurements allow for the first accurate comparison of the collocated RID and RSD. The resolutions of the refractive index and stress are estimated to be 2.34×10^{-5} and 0.35 MPa, respectively. © 2012 Optical Society of America

OCIS codes: 060.2270, 060.2310, 060.2400, 110.0180.

1. Introduction

Optical fiber technology continues to advance rapidly as a result of the increasing demands on communication systems and the growing field of fiber-based sensing. New optical fiber types to control loss, dispersion, and nonlinear effects are required to permit higher data rates, more channels in wavelength-division multiplexing systems, and more flexible installation requirements to bring optical signals closer to the end user [1,2]. Fiber-based communication components enable crucial signal manipulation capabilities, including coupling, filtering, and amplification [3]. Fiber-based sensors are continually being developed for a broad range of sensing applications, including environmental, medical, structural, industrial, and military. Sensors that use the intrinsic properties of the fiber as a sensing mechanism, referred to as intrinsic fiber-based sensors, possess the inherent advantages of optical fibers. They are small in size, immune to electromagnetic interference, resistant to many hazardous chemicals, and capable of remote monitoring. Furthermore, fibers are readily available because of the vast extent of the telecommunications industry. As optical fibers and fiber-based devices continue to advance, the need to understand their fundamental physical properties simultaneously increases. Physical properties, such as size, refractive-index distribution (RID), and residual-stress distribution (RSD), affect the performance of optical fibers and are important for modeling, design, and evaluation.

The RID in an optical fiber is fundamental in determining its transmission properties. In fibers with azimuthally symmetric RIDs, the step-index profile provides the simplest design. However, graded-index designs are necessary to minimize the differential group delay in multimode fibers. In single-mode fibers, RIDs with graded-index, multistep, triangular-core, and trapezoidal-core designs are used to minimize loss, control mode-field distributions, and

1559-128X/12/225442-11$15.00/0

control dispersion [4]. New fiber types with larger mode-field areas allow for increased input powers while maintaining sufficiently low intensities to avoid nonlinear effects [1]. RIDs with low-index trenches in the cladding greatly reduce bending losses to permit relaxed installation requirements for applications such as fiber-to-the-home [2]. Azimuthally asymmetric RIDs, such as elliptical-core designs, are used to make polarization-maintaining fibers.

The RID is also important in fiber-based communication components and sensors. The custom design of RIDs can provide gain-flattened, broadband Raman amplifiers without the need for multiple pumps [5]. The azimuthally asymmetric perturbations to the RID in CO_2-laser-induced long-period fiber gratings (LPFGs) enable wavelength tuning and attenuation tuning by varying the bend radius and the azimuthal orientation of the bend direction [6–9]. Asymmetric perturbations also allow for directional bend- and load-sensing behaviors [10,11].

The RSD is known to affect both the transmission properties and the physical properties of optical fibers [12–15]. The presence of residual stresses can be detrimental in many applications. However, the careful addition or modification of residual stresses can also enable numerous new applications. The presence of residual tensile stresses near the surface of an optical fiber can lead to cracking and a decreased lifetime [16,17]. Crack formation can be reduced, however, if compressive stresses are frozen in near the surface of the fiber [18]. Stress-induced birefringence in optical fibers is detrimental to systems that require low polarization sensitivity [19] or low polarization-mode dispersion [4,20–22]. However, residual stresses are necessary to create the high birefringence required for certain types of polarization-maintaining fibers [4,23]. The relaxation of residual stresses that results from cleaving a fiber can cause unexpected changes in performance [24].

The controlled modification of residual stresses enables the fabrication of several types of fiber-based devices. Changes in the RSD in various fiber types have been observed in fiber Bragg gratings (FBGs) [25–27] and LPFGs [28–32] fabricated by various techniques. RSD modification is also hypothesized to contribute to the RID changes necessary for beam expansion in high-power connectors [33].

It is evident that the RID and the RSD have a fundamental effect on the performance of optical fibers, both optically and mechanically. The knowledge of these fundamental physical properties is necessary for modeling, design, and evaluation. This need continues to increase as the demands on optical fibers and fiber-based devices rise and designs become more complex. There are several requirements that must be met by measurement techniques to characterize suitably the RID and the RSD in optical fibers. First, the techniques must be capable of measuring three-dimensional distributions without the need to make assumptions about symmetries or uniformities in the fiber. Second, the techniques must be suitably accurate to characterize the small variations in the RID and the RSD. Third, because the RID and the RSD are inherently linked by the photoelastic effect, the techniques must be capable of characterizing these properties concurrently. The RID and the RSD must be characterized in the same location of an optical fiber or fiber-based device to enable accurate comparison. Fourth, the techniques must be nondestructive. Destructive techniques not only perturb and destroy the optical fiber or fiber-based devices, but they also eliminate the possibility of performing concurrent measurements of the RID and the RSD.

The important requirement for nondestructive measurements cannot be met by many existing characterization techniques, most notably, techniques that require access to the end-face of the optical fiber. However, there are several techniques that exist for characterizing the RID and the RSD nondestructively. Interferometric techniques, such as microinterferometric optical phase tomography [34,35], phase-shifting interferometry [36], and dispersive Fourier-transform spectroscopy [37], can be used with computed tomography principles to characterize three-dimensional RIDs. Photoelastic techniques, such as polarization-digital-holographic microscopy [38] and phase-stepping or phase-shifting photoelasticity [39,40], and phase modulation techniques [41], can be used with computed tomography principles to characterize three-dimensional RSDs. All of these techniques, however, require the use of specialized equipment, such as interference microscopes, multiple waveplates in multiple or single beam paths, and custom phase modulators. These requirements make concurrent characterization of the RID and the RSD, and thus accurate comparison of these properties, prohibitively difficult.

Quantitative-phase microscopy (QPM) has been demonstrated to be capable of providing three-dimensional, concurrent, nondestructive characterization of the RID and the RSD in optical fibers. QPM is a noninterferometric technique that enables the determination of the phase shift produced by the fiber [42]. This technique uses a standard microscope-based configuration to obtain an in-focus image of the fiber and two slightly defocused images on either side of the in-focus position. The phase shift induced by fiber can be determined by (1) using the defocused images to estimate the derivative of the intensity in the beam-propagation direction (longitudinal intensity derivative) and then (2) solving numerically the transport of intensity equation (TIE) [43]. Computed tomography principles have been used with this technique to determine azimuthally asymmetric RIDs [44].

Because the QPM technique enables the determination of the phase shift, it can also be used to characterize the RSD by measuring directly the retardation produced by an optical fiber [45,46]. This requires a polarizer on the light source to characterize independently the phase shifts produced by the

fast and slow indices of the fiber. The difference in the phase shift produced by the fast and slow indices is the retardation. However, the determination of the phase shifts requires the measurement of relative intensity distributions (in-focus and defocused images). This is, in general, not as accurate as detecting a minimum of intensity and limits the minimum detectable retardation. It has been shown that this technique is limited to detecting retardations on the order of $\lambda/10$, which is an order of magnitude higher than the low retardations (on the order of $\lambda/100$) produced by typical optical fibers [46–48].

The existing techniques for characterizing the RID and the RSD in optical fibers are not capable of one or more of the following requirements: (1) measuring three-dimensional distributions without the need to make assumptions about symmetries or uniformities, (2) measuring accurately the small variations in the RID and the RSD, (3) measuring concurrently the RID and the RSD, and (4) measuring nondestructively. Without meeting these requirements, the existing techniques are limited in providing insight into the effects of the RID and the RSD on the performance of optical fibers, both optically and mechanically, and are limited in providing useful information for modeling, design, and evaluation.

In this paper, we present a new three-dimensional index-stress distribution (3DISD) measurement method to meet all of the requirements for characterizing the RID and the RSD in optical fibers and fiber-based devices. This method combines the use of the QPM technique, the Brace–Köhler compensator (BKC) technique, and computed tomography principles. The QPM technique provides measurements of the phase shift produced by an optical fiber. When combined with computed tomography principles, this technique provides accurate characterization of the three-dimensional RID [44,49–51]. The BKC technique provides accurate measurements of the low levels of retardation produced by an optical fiber and, when combined with computed tomography principles, provides accurate characterization of the three-dimensional RSD [47,48]. Furthermore, both techniques enable the use of a commercial microscope. This feature not only takes advantage of robust, commercial design, but also enables the concurrent characterization of the RID and the RSD. The optical fiber does not need to be moved between separate pieces of equipment to measure both properties. Therefore, for the first time, an accurate comparison of the RID and the RSD and their interdependence can be made.

The theories, measurement procedures, experimental apparatus, and data analysis techniques for the BKC technique are discussed in detail in [47,48]. The theories, measurement procedures, experimental apparatus, and data analysis techniques for the QPM technique are discussed in Section 2. Also discussed in this section is the experimental determination of the optimal measurement parameters for characterizing optical fibers with the QPM technique. Improvements to the BKC technique are discussed in Section 3. Concurrently characterized RIDs and RSDs in Corning SMF-28 fiber in (1) an unperturbed section and (2) a section exposed to focused pulses of carbon-dioxide (CO_2) laser radiation are presented in Section 4. This section also includes an assessment of the performance of the techniques. The results are summarized in Section 5.

2. RID Characterization

A. Phase-Shift Measurement

An Olympus BX-60 microscope with additions to enable partial measurement automation is used to implement the QPM technique. A diagram of the relevant optical components is shown in Fig. 1. Illumination is provided by a mercury-arc lamp and a 546 nm interference filter with a FWHM of 10 nm. The use of an incoherent source eliminates interference effects due to the diffraction of a coherent source, such as an HeNe laser. A strain-free, polarizing condenser and a strain-free 40× objective with a numerical aperture (NA) of 0.75 provide high-magnification imaging. The polarizer and condenser are integrated into one housing, allowing for the precise alignment of both optical components.

A measurement consists of first placing the fiber sample in the microscope for transverse illumination; the direction of the propagation of the illuminating beam, z_m, is normal to the longitudinal axis of the fiber. The fiber is oriented in the $x_m y_m$ plane at 45° from the polarizer. The linear polarization of the light transmitted through the birefringent fiber is

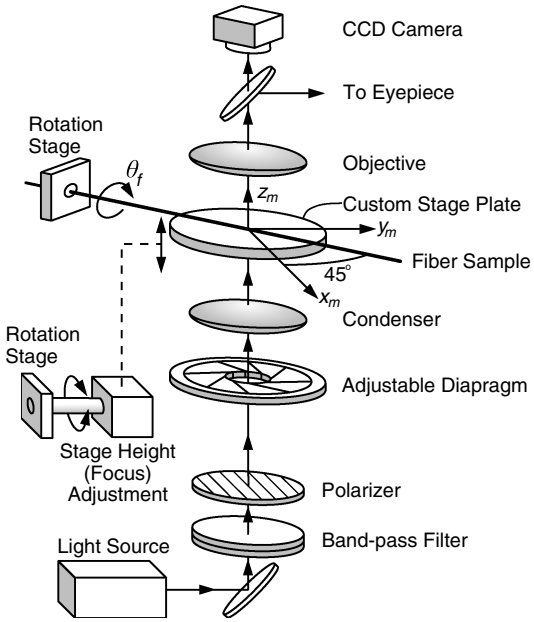

Fig. 1. Configuration of the components of the microscope and a fiber sample used for the determination of the phase shift produced by the fiber. Axial rotation of the fiber between measurements is indicated by θ_f. Focusing and defocusing of the fiber is achieved by moving the stage plate of the microscope in the vertical direction, z_m.

split between the principal axes, which are defined as the longitudinal axis and the radial axis. The accuracy of the QPM technique is not sufficient to detect the difference in the phase shift induced by the two orthogonal polarizations in typical optical fibers. Therefore, a combination of the transverse and longitudinal indices is detected.

By assuming that refraction is minimal, the intensity distribution, I, and the phase-shift distribution, φ, of the light transmitted through the fiber are related by the TIE

$$-\frac{2\pi}{\bar{\lambda}}\frac{\partial I}{\partial z_m} = \nabla_\perp \cdot (I\nabla_\perp \varphi), \tag{1}$$

where $\bar{\lambda}$ is the mean wavelength of the light source and $\nabla_\perp = \frac{\partial}{\partial x_m} + \frac{\partial}{\partial y_m}$ [42,44]. The phase shift, φ, is defined as the difference in the phase accumulated by the light transmitted through the fiber and the phase accumulated by the light transmitted through the medium surrounding the fiber. The intensity and phase-shift distributions are in the transverse plane of the fiber, or the $x_m y_m$ plane as indicated in Fig. 1. Therefore, the intensity is observed through the eyepiece or by the CCD when the fiber is in focus and the longitudinal derivative of the intensity, $\partial I/\partial z_m$, is observed by defocusing the fiber. Here longitudinal refers to the direction of propagation of the illuminating beam in the microscope, z_m. Defocusing is achieved by moving the stage plate of the microscope in the vertical direction (z_m) as indicated in Fig. 1. Automated focusing and defocusing of the fiber is achieved by rotating the fine focus knob on the microscope with a computer-controlled rotation stage (Newport model SR50PP) coupled to the focus knob.

The in-focus intensity distribution is obtained by capturing an image of the fiber when it is in focus. The longitudinal derivative of the intensity is approximated using the central difference formula by capturing two defocused images of the fiber: one defocused above and one defocused below the in-focus position. With these three images, the TIE, Eq. (1), can be solved numerically for the phase-shift distribution.

The determination of cross-sectional RIDs requires phase-shift measurements for angular orientations of the fiber, θ_f, spanning $0 \le \theta_f < 180$ deg. The measurements are made at various angles by rotating the fiber about its longitudinal axis within the microscope. After the first phase-shift measurement at $\theta_f = 0$, the fiber is rotated by a small amount. The focus and the positioning of the fiber are checked; occasionally radial runout requires the fiber to be refocused and/or recentered within the field of view (FOV). A phase-shift measurement is then performed at the new rotation angle. The process of rotating the fiber and performing a measurement is repeated until the fiber has been rotated 180°. The fiber is rotated in increments of 2°, which corresponds to 89 phase-shift measurements.

B. RID Determination

Computed tomography principles enable the determination of the cross-sectional RID from a sequence of phase-shift profiles obtained over 180° of rotation of the optical fiber. By inspection of Fig. 2, the phase shift of a beam passing at an angle θ_f through the fiber can be written as

$$\varphi(x', \theta_f) = \frac{2\pi}{\lambda}\int_{-\infty}^{\infty} \Delta n(x', y')\mathrm{d}y', \tag{2}$$

where λ is the wavelength of the light source and $\Delta n(x', y') = n(x', y') - n_{\text{oil}}$ is the relative refractive index.

For each rotation angle of the fiber, θ_f, the Fourier slice theorem states that the one-dimensional Fourier transform of the phase-shift profile, $\tilde{\Phi}$, is equal to a radial slice of the two-dimensional Fourier transform of the cross-sectional RID (multiplied by $\frac{2\pi}{\lambda}$), $\frac{2\pi}{\lambda}\Delta\tilde{N}$. Defining s as the spatial angular frequency, this theorem is expressed as

$$\tilde{\Phi}(s, \theta_f) = \frac{2\pi}{\lambda}\Delta\tilde{N}(s\cos\theta_f, s\sin\theta_f), \tag{3}$$

where the coordinates $(s\cos\theta_f, s\sin\theta_f)$ define a slice at an angle θ_f through the spatial angular frequency domain.

With phase-shift profiles spanning $0 \le \theta_f < 180$ deg, the entire cross-sectional RID can be determined using this theorem. However, the direct implementation of Eq. (3) requires the phase-shift profiles obtained in polar coordinates to be mapped to rectangular coordinates. This requires interpolation in the spatial angular frequency domain. Interpolation of spatial angular frequencies will affect all points in the real spatial domain, leading to interpolation errors across the entire index distribution. To avoid frequency-domain interpolation, filtered backprojection can be used to implement the Fourier slice theorem [52].

By taking the inverse two-dimensional Fourier transform of Eq. (3) and by recognizing that phase-shift

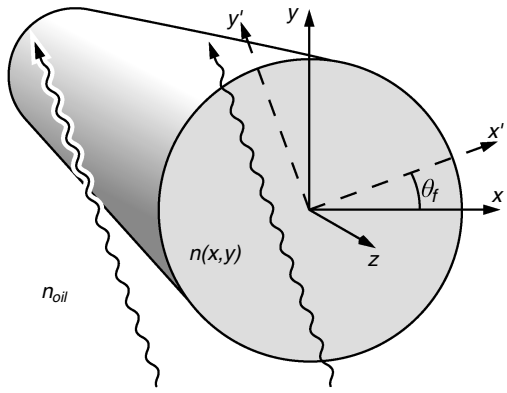

Fig. 2. Configuration of fiber illumination for phase-shift measurements.

profiles taken 180° apart are mirror images, the relative RID can be expressed as

$$\Delta n(x',y') = \frac{\lambda}{2\pi}\int_0^{\pi}\left[\int_{-\infty}^{\infty}\tilde{\Phi}(s,\theta_f)|s|e^{i2\pi sx'}\mathrm{d}s\right]\mathrm{d}\theta. \quad (4)$$

The quantity $\tilde{\Phi}(s,\theta_f)|s|$ is the Fourier transform of a measured phase-shift profile multiplied by a ramp in the spatial angular frequency domain. In practice, the ramp filter may be modified for better performance with noisy data. Equation (4) is a form of the inverse Radon transform and permits the determination of the cross-sectional RID from phase-shift profiles.

The determination of a cross-sectional RID from the measured phase-shift distributions requires three primary steps: (1) the extraction of a single radial profile of the phase shift from each distribution, (2) the alignment of the profiles, and (3) the calculation of the RID. These steps are analogous to the steps required for the determination of RSDs, which are discussed in detail in [47,48].

C. Optimal Measurement Parameters

The QPM technique requires the careful selection of the NA of the condenser and the defocus distance used to obtain the defocused images of the optical fiber [53]. The *a priori* optimal settings for the condenser NA and the defocus distance for the characterization of optical fibers are not clear. Furthermore, tradeoffs exist for selecting these parameters. The condenser NA affects the coherence of the light that illuminates the fiber [53]. A higher NA results in less coherent illumination, which can improve the spatial resolution of the microscope. However, a lower NA results in more coherent illumination, which improves the spatial resolution of the longitudinal intensity derivative, and thus the spatial resolution of the phase shift. The defocus distance must be small enough to provide an accurate approximation of the longitudinal change in the intensity, $\partial I/\partial z_m$, but it must be large enough to enable the detection of changes in the intensity in the presence of noise [53,54]. In addition to degrading the approximation of $\partial I/\partial z_m$, a larger defocus distance results in the blurring of the intensity distribution by the increasingly visible effects of diffraction. Reports of the determination of the refractive-index profiles (RIPs) and the RIDs in fibers specify defocus distances of 2–3 μm with a 40× objective [46,55].

The optimal settings of the condenser NA and the defocus distance were determined by (1) quantifying the repeatability of the phase-shift measurements and (2) assessing qualitatively the resulting RIPs. As mentioned previously, numerous phase-shift measurements at various angular orientations of the fiber are necessary to use computed tomography principles to determine RIDs. Accurate determination of the RIDs requires repeatable phase-shift measurements. Preliminary measurements were performed to determine the optimal condenser NA and the optimal defocus distance for the repeatable characterization of optical fibers. The relative RIP, $\Delta n(r) = n(r) - n_{\mathrm{oil}}$, of an unperturbed Corning SMF-28 fiber was characterized. The term relative is omitted in the remainder of this paper, but all references to and measurements of RIPs and RIDs refer to the relative refractive index. The RIP, rather than the full RID, was determined to assess rapidly the effect of changing the condenser NA and the defocus distance. The fiber was surrounded by a light mineral oil with an unknown index of refraction with a value between the indices of the core and the cladding of the fiber.

Single phase-shift measurements were performed with condenser NAs of 0.1, 0.2, 0.4, and 0.6 and defocus distances of 1, 2, and 3 μm. The RIP was calculated from the phase shift using a Fourier-based algorithm to compute the inverse Abel transform [56]. A set of 10 identical measurements (referred to as a measurement set) was performed for each combination of the condenser NA and the defocus distance. For each measured RIP, the step-index difference of the fiber was determined. The step-index difference is defined as $\Delta n_s = n_{\mathrm{core}} - n_{\mathrm{clad}}$, where n_{core} is the maximum measured refractive index in the core region and n_{clad} is the average measured refractive index in the cladding region. The repeatability of each combination of the condenser NA and the defocus distance is assessed by determining the standard deviation in the step-index difference for each measurement set.

The standard deviations of the measured step-index differences are shown in Table 1. In general, larger defocus distances, which improve the detection of changes in the intensity in the presence of noise, provide more repeatable measurements. While these results indicate that a larger defocus distance is optimal, the choice of a maximum defocus distance and the condenser NA is less clear. To determine the maximum defocus distance and optimal condenser NA, a qualitative analysis of the RIPs was performed. It was observed that while the repeatability continued to improve for defocus distances greater than 3 μm, the improvements were small and accompanied by a more significant degradation to the spatial resolution of the RIPs. This is a result of larger defocus distances leading to (1) the degradation of the approximation of $\partial I/\partial z_m$ and (2) the blurring of the intensity distribution by the increasingly visible effects of diffraction [53,54]. Therefore, 3 μm is determined to be the optimal defocus distance.

Table 1. Percent Standard Deviation in Δn_s for 10 Identical Measurements

	NA$_c$			
δz_m (μm)	0.1	0.2	0.4	0.6
1	5.66%	4.44%	3.63%	5.51%
2	1.94%	2.94%	1.64%	2.14%
3	2.12%	1.07%	1.61%	1.36%

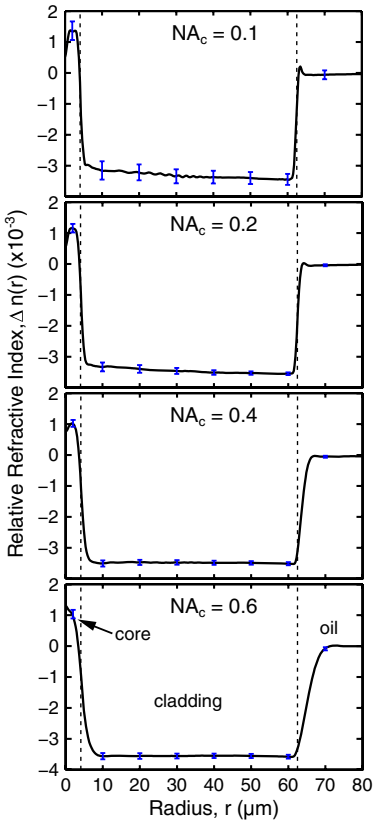

Fig. 3. (Color online) Average RIPs of an unperturbed Corning SMF-28 fiber obtained using the QPM technique with a defocus distance of 3 μm and various condenser NAs, NA$_c$. Each RIP is the average of 10 measurements. The error bars indicate the standard deviation of the average RIP at positions of $r = 2$, 10, 20, 30, 40, 50, 60, and 70 μm. The dotted lines indicate the core radius (4.1 μm) and the cladding radius (62.5 μm) of a Corning SMF-28 fiber.

The average RIPs for each condenser NA and a defocus distance of 3 μm are shown in Fig. 3. The profiles obtained with low condenser NAs have a less uniform cladding refractive index than the profiles obtained with higher NAs. However, the profiles obtained with higher NAs show a more gradual change at the boundaries between the various regions of the fiber. These gradual changes indicate that a higher condenser NA results in a degraded spatial resolution of the longitudinal intensity derivative, and thus a degraded spatial resolution of the resulting RIP. Based on these observations, it is determined that a condenser NA of 0.4 is necessary to (1) provide an accurate measurement of the RIP as indicated by the uniform cladding, and (2) avoid any unnecessary degradation in the spatial resolution.

In addition to the requirement of repeatable phase-shift measurements, accurate determination of RIDs using computed tomography principles requires repeatable focusing of the optical fiber from measurement to measurement. The automated control of the fine focus knob provides repeatable defocusing of the fiber. However, the in-focus position of the fiber must be found manually. The radial runout

Table 2. Percent Standard Deviation in Δn_s for Measurements with Intentional In-Focus Position Error

	NA$_c$			
δz_m (μm)	0.1	0.2	0.4	0.6
1	5.14%	4.09%	5.16%	4.94%
2	2.77%	3.83%	2.17%	2.47%
3	1.51%	1.28%	1.19%	1.30%

of the fiber during rotation leads to defocusing and occasionally requires finding a new in-focus position. Therefore, the effect of variability in finding the in-focus position was investigated.

The effect of varying the in-focus position, z_{m0}, was determined by performing measurements with an intentional error in the in-focus position; the in-focus position was set intentionally to a position other than the position of best focus, $z_{m,bf}$. A set of 12 measurements was performed for each combination of the condenser NA and the defocus distance: four measurements with the correct in-focus position ($z_{m0} = z_{m,bf}$), four with the in-focus position offset by -0.5 μm ($z_{m0} = z_{m,bf} - 0.5$ μm), and four with the in-focus position offset by $+0.5$ μm ($z_{m0} = z_{m,bf} + 0.5$ μm). The defocus distance remained constant for each measurement set. The standard deviations of the step-index differences that were measured with the intentional in-focus position errors are shown in Table 2. The standard deviations are similar to those presented in Table 1. Several of the standard deviations for the measurement sets with the intentional in-focus position error are lower than the measurement sets with a consistent in-focus position. This result indicates that small variations in the in-focus position between measurements are negligible for any setting of the defocus distance and condenser NA. A consistent defocus distance and condenser NA from measurement to measurement, rather than the repeatability of obtaining the best in-focus position, is the crucial parameter.

3. RSD Characterization

The Olympus BX-60 microscope used for the phase-shift measurements is also used to implement the BKC technique. The use of one experimental apparatus to perform the measurements is necessary to characterize concurrently the RID and the RSD. This eliminates the need to move the optical fiber between separate pieces of equipment and enables the accurate comparison of the RID and the RSD. The objective, the orientation of the fiber in the microscope, and the orientation of the polarizer are the same for both measurements. Furthermore, the retardation measurements are made at the same angular orientations of the fiber used for the phase-shift measurements (Subsection 2.A). The condenser NA is set to 0.6 for the retardation measurements, which is 80% of the objective NA (0.75), to ensure high-quality Köhler illumination. The theories, measurement procedures, experimental apparatus, and data analysis techniques for the characterization of RSDs

using the BKC technique are discussed in detail in [47,48]. However, two improvements have subsequently been made to the experimental apparatus and the data analysis procedures.

First, the CCD camera used to capture digital images of the optical fiber is now a QImaging Retiga 1300R configured to capture 12 bit gray-scale images. This camera offers an improved bit depth for capturing the low-intensity images produced with the BKC technique over the previously used 8 bit CCD [48]. Second, the procedure for analyzing the captured images to determine the retardation has changed. The retardation produced by the fiber is determined for each angular orientation by analyzing a sequence of images that records the variation in the intensity with changing compensator angle. For each pixel, the compensator angle that produces a minimum of intensity is determined by fitting the variation in intensity with an nth-order polynomial and determining the location of the minimum of the polynomial.

Previously, the order of the polynomial was chosen based on the standard deviation of the difference between the fit and the experimental variation in intensity. Typically, a fifth-order polynomial was used. However, it was determined that while a higher-order polynomial provided a lower standard deviation, the least-squares fitting technique resulted in a polynomial that fit to the experimental noise. This resulted in a greater deviation in the compensator angle that produces a minimum of intensity, which subsequently resulted in a greater deviation in the calculated retardation. A second-order polynomial is used for the results presented in this paper, which provides a fit that does not vary with the experimental noise. The improvement in the deviation in the measured retardation is discussed in Subsection 4.C.

4. Results

A. Unperturbed Fiber

The RID and the RSD were concurrently characterized in an unperturbed Corning SMF-28 fiber. The relative RID, $\Delta n(x,y) = n(x,y) - n_{\text{oil}}$, was measured using the optimal condenser NA of 0.4 and the optimal defocus distance of 3 μm. The fiber was surrounded by an index matching oil from Cargille Labs (series AA, $n_D = 1.4580$). The measurements were performed at a room temperature of approximately 23–24 °C. The RSD was determined as described in [47,48] with the improvements discussed in Section 3. A typical cross-sectional RID–RSD pair is shown in Fig. 4.

The three-dimensional plot of the RID shows that the expected step-index profile is reconstructed. Slightly visible in the three-dimensional plot and clearly visible in the inset pseudocolor plot of the core is a region of lower refractive index in the center of the core. This region is referred to as the center dip or burn-off region. The decrease in the refractive index is a consequence of the internal vapor deposition used to manufacture the core preform [57]. In the final stage of collapsing the tube to form the core preform, some of the dopant gas is not deposited on the innermost layer, resulting in a lower index of refraction in the center of the core. This center dip has been measured in the same type of fiber by other techniques and indicates sufficient spatial resolution to characterize this small feature [35,37].

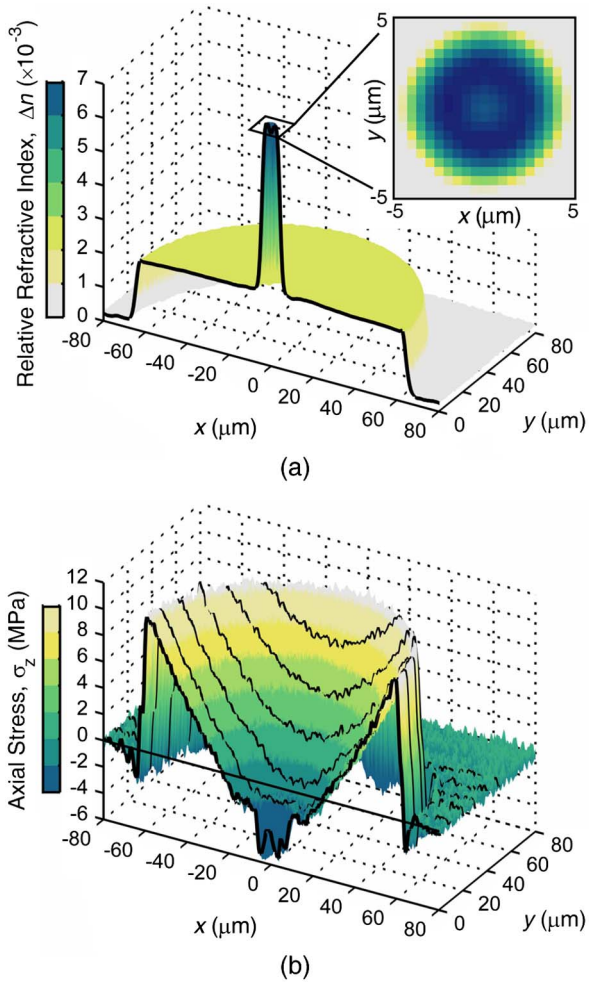

Fig. 4. (Color online) Plots of (a) a typical cross-sectional RID and (b) a typical cross-sectional RSD in an unperturbed Corning SMF-28 fiber. The inset in (a) is a pseudocolor plot of the core showing the central dip or burn-off region. The pseudocolor scale on the inset ranges from $4 - 7 \times 10^{-3}$. Line profiles of the RSD (b) are shown for $x = 0$, 10, 20, 30, 40, and 50 μm.

The three-dimensional plot of the RSD agrees well with the initial measurement reported in [47] and [48]. This measurement validates the 3DISD method and provides a means to quantify the improvements discussed in Section 3. The effects of both mechanical stress and thermal stress are seen in the unperturbed fiber and are discussed in detail in [47]. In addition, the RSD reveals a net tensile stress in the fiber. The mean axial stress in the unperturbed Corning SMF-28 fiber is +4.70 MPa, indicating a mean axial tension [47]. However, in the absence of external forces, the mean stress in the fiber should be zero.

The apparent nonzero mean stress has been hypothesized to be caused by the presence of inelastic

strain birefringence that exists in the fiber along with stress-induced birefringence, which can be equivalently referred to as elastic strain birefringence. Stress-induced birefringence arises because residual stresses remain in the fiber after it is drawn and without the presence of externally applied forces [15]. Inelastic strain birefringence is hypothesized to result from frozen-in viscoelasticity [15,58]. Viscoelasticity refers to the time- and temperature-dependent relaxation, or contraction, of the molten glass during the drawing process. Frozen-in viscoelasticity refers to an incomplete contraction of the glass during the drawing process. In general, while the glass is molten, and thus viscoelastic, the glass contracts more in the transverse direction and less in the axial direction because of the draw tension. The glass then solidifies with a positive strain and thus a positive birefringence. This strain is frozen into the glass structure independent from the residual stresses that exist and is thus referred to as inelastic strain birefringence [15].

The apparent nonzero mean stress was measured in the unperturbed fiber because both types of birefringence were characterized with the BKC measurement technique (or any photoelastic technique) [59]. The measured retardation in the fiber is due to birefringence. The birefringence is then related to the stress through the stress-optic law. However, the stress-optic law is only valid for stress-induced birefringence. The presence of inelastic strain birefringence also enters into the measured retardation, and thus it affects the calculated stress. The apparent mean axial tension in the unperturbed fiber is due to the measurement of not only the stress-induced birefringence, but also the inelastic strain birefringence.

Durr *et al.* showed that if the inelastic strain is assumed to be spatially uniform throughout the fiber, then its value can be determined experimentally from the measured mean axial stress [60]. The inelastic strain determined in this way agreed with the predicted inelastic strain for fibers drawn with various draw tensions. This suggests that the actual residual axial stress in an unperturbed fiber can be determined by subtracting the mean axial stress from the measured axial stress.

B. Fiber Exposed to CO_2 Laser Radiation

The ability to characterize fibers with azimuthal and longitudinal variations was verified by characterizing concurrently the cross-sectional RID and RSD in a section of Corning SMF-28 fiber exposed from one side to a focused, 500 ms duration pulse from a CO_2 laser. The fiber was exposed using an LPFG fabrication apparatus described in [9]. The 500 ms pulse duration was chosen to match the duration typically required to fabricate each period of an operational LPFG.

Pairs of relative RIDs, $\Delta n(x,y,z) = n(x,y,z) - n_{\text{oil}}$, and RSDs, $\sigma_z(x,y,z)$, at various longitudinal positions, z, in the exposed section of the fiber are shown in Fig. 5. The distributions at $z = 0$ μm correspond approximately to the longitudinal center of the exposure to the focused CO_2 laser. The distributions at $z = -150$ μm and $z = 150$ μm are approximately 10 μm from the edge of the microscope FOV. The azimuthal asymmetry of the RIDs and the RSDs in the exposed section is clear in Fig. 5. This asymmetry is expected because of the one-sided exposure to the laser. The arrows below the $z = 0$ distributions in Fig. 5 indicate the direction of the exposure. The absorption of higher intensities results in more heating on the side of the fiber facing the exposure, and thus asymmetric changes are produced.

The asymmetry in the RID is stronger than the asymmetry in the RSD. This is a result of the differing processes that produce the changes in the refractive index and the stress [61]. The changes in the

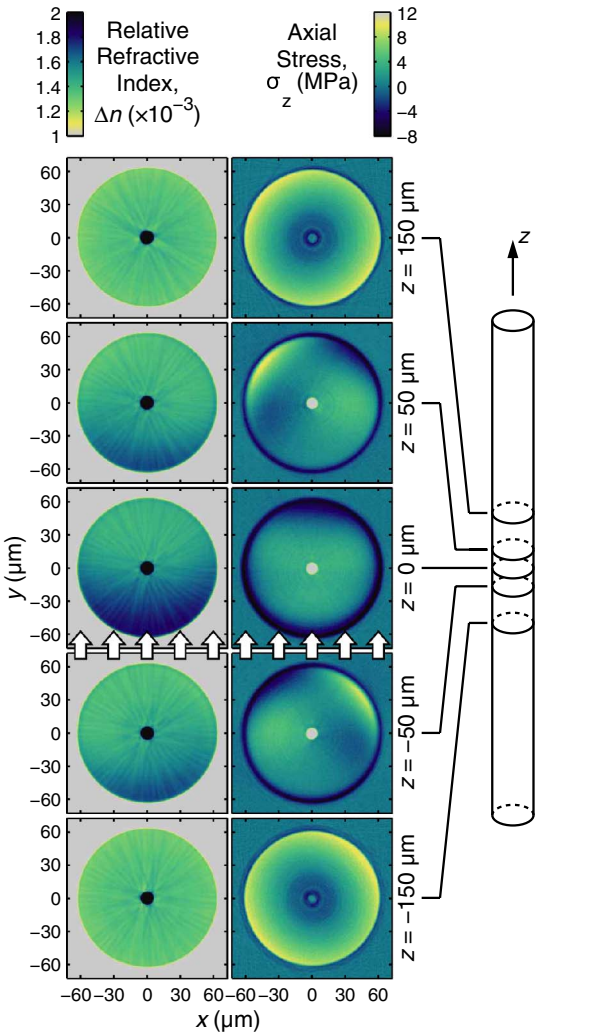

Fig. 5. (Color online) Relative RIDs (left column) and RSDs (right column) at various longitudinal positions in a section of Corning SMF-28 fiber exposed to a focused, 500 ms duration pulse from a CO_2 laser. The position $z = 0$ corresponds approximately to the center of the exposure. The fiber diagram indicates the approximate spacing between the longitudinal positions relative to the fiber diameter. The arrows below the $z = 0$ distributions indicate the exposure direction.

refractive index are caused primarily by the densification of the fiber on side facing the exposure. This increase in the density of the glass, and thus the refractive index, is produced by CO_2-laser-induced annealing (relaxing) of frozen-in viscoelasticity formed during the fiber drawing process [58]. The changes in the stress, however, are caused primarily by the relaxation of mechanically induced stresses. The mechanically induced stresses are relaxed throughout the fiber revealing the unaffected thermally induced stresses [28]. These measurements indicate the capability of the 3DISD method to measure azimuthal asymmetries and longitudinal variations in the RID and the RSD of an optical fiber. The effects of the focused CO_2 laser pulses on LPFG fabrication are discussed in more detail in [61].

C. Assessment of Techniques

As discussed in [48], no absolute standard of comparison for this type of measurement exists. However, several figures of merit can be used to assess the performance of the presented techniques and apparatus. These figures of merit also provide a basis of comparison with other techniques as well as for future development and improvements. The performance of the index characterization technique and apparatus is assessed in a manner analogous to that used for the stress characterization technique and apparatus discussed in [48]. The performance is evaluated in terms of the lateral spatial resolution, the noise present in the determined phase shift, and the noise present in the determined RID.

The lateral spatial resolution of the measurement apparatus, which is determined by imaging optics, is about 0.58 μm for the phase-shift measurements and about 0.49 μm for the retardation measurements. The larger resolution for the phase-shift measurements is a result of the smaller condenser NA. These resolutions indicate the spatial resolution of the RIDs and RSDs along the fiber axis; however, the transverse resolution is affected by the measurement procedures and computed tomography principles used to determine the RIDs and RSDs. The blurring of edges with large transitions is caused by the filtered-backprojection algorithm used to perform the computed tomography [47,62].

The noise present in the phase shift is determined from the standard deviation of the phase shift in the region surrounding the fiber (surrounding-region phase shift). The average standard deviation of the surrounding region of all the phase-shift distributions obtained for the unperturbed Corning SMF-28 fiber is 2.84 nm (at $\lambda = 546$ nm). This value provides an estimate of the phase-shift resolution. The noise present in the RID is obtained by calculating the standard deviation of the cross-sectional RID in the region surrounding the fiber. However, only an annular ring between the outer cladding edge and a circle inscribing the RID data is considered [48]. The standard deviation of the RID in the annular-ring region surrounding the fiber is 2.34×10^{-5}. Thus, the noise in the RID determined with the presented technique is estimated to be $\pm 2.34 \times 10^{-5}$. This value provides an estimate of the refractive-index resolution.

The performance of the stress characterization technique was initially reported in [48]. However, the performance was reassessed after the improvements discussed in Section 3. The noise present in the retardation is determined from the standard deviation of the retardation in the region surrounding the fiber (surrounding-region retardation). The average standard deviation of the surrounding region of all the retardation distributions obtained for the unperturbed Corning SMF-28 fiber is 0.013 nm (at $\lambda = 546$ nm). This is a 78% improvement from the 0.058 nm obtained from the initial measurement reported in [47] and [48] (reported as 0.06 nm). The improvement is attributed to (1) the more appropriate quadratic-polynomial-fit interpolation procedure discussed in Section 3 and (2) the better performance of the QImaging CCD camera relative to the camera reported in [48]. Further analysis of the retardation distributions reveals a noise level throughout the fiber that is similar to the noise in the surrounding region. Therefore, the noise in the retardation determined with the improved technique and apparatus is estimated to be ± 0.013 nm. This value provides an estimate of the retardation resolution.

The noise present in the RSD is obtained by calculating the standard deviation of the cross-sectional RID in the annular-ring region surrounding the fiber. The standard deviation of the RSD in the annular-ring region surrounding the fiber is 0.35 MPa. This is a 68% improvement from the 1.10 MPa obtained from the initial measurement reported in [48]. This improvement is also attributed to (1) the more appropriate quadratic-polynomial-fit interpolation procedure and (2) the better performance of the QImaging CCD camera. Further analysis of the RSD reveals a noise level throughout the fiber that is similar to the noise in the surrounding region. Thus, the noise in the RSD determined with the presented technique is estimated to be ± 0.35 MPa. This value provides an estimate of the axial stress resolution.

5. Summary

A 3DISD measurement method for determining concurrently the three-dimensional RIDs and RSDs in optical fibers and fiber-based devices has been developed. The method combines the QPM phase-shift measurement technique and the BKC retardation measurement technique and implements them on a common measurement apparatus. This enables the accurate measurement of the RID and the RSD without the need to move the optical fiber between separate pieces of equipment. A sequence of measurements with various settings of the condenser NA and the defocus distance reveal that a condenser NA of 0.4 and a defocus distance of 3 μm are optimal for characterizing the RID optical fibers with the current apparatus.

The 3DISD measurement method was used to characterize the RID and the RSD in a Corning SMF-28 fiber in an unperturbed section and a section exposed to CO_2 laser radiation. The measurement of the RID in the unperturbed section resolved the center dip in the core of the fiber that results from dopant burn off. The measurement of the RSD agrees well with an initial measurement reported in [47] and [48]. The measurements of the exposed section of the fiber provide the first concurrent evidence of the changes that occur in the RSD and the RID during LPFG fabrication. These measurements also validate the capability to measure small, asymmetric changes in the RID and the RSD.

An analysis of the region surrounding the fiber was used to determine the noise in the measured phase shift, refractive index, retardation and axial stress. The noise in the phase shift was calculated to be ± 2.84 nm (at $\lambda = 546$ nm), and the noise in the refractive index was calculated to be $\pm 2.34 \times 10^{-5}$. Similarly, the noise in the retardation was calculated to be ± 0.013 nm (at $\lambda = 546$ nm), and the noise in the axial stress was calculated to be ± 0.35 MPa. While no standard of comparison exists for these types of measurements, these figures of merit provide a provide a basis of comparison with other techniques as well as for future development and improvements.

References

1. J. Yu and X. Zhou, "Ultra-high-capacity DWDM transmission system for 100G and beyond," IEEE Commun. Mag. **48**, S56–S64 (2010).
2. P. R. Watekar, S. Ju, and W. T. Han, "Design and development of a trenched optical fiber with ultra-low bending loss," Opt. Express **17**, 10350–10363 (2009).
3. L. Eldada, "Optical communication components," Rev. Sci. Instrum. **75**, 575–593 (2004).
4. J. A. Buck, *Fundamentals of Optical Fibers* (Wiley, 2004).
5. A. C. O. Chan and M. Premaratne, "Dispersion-compensating fiber Raman amplifiers with step, parabolic, and triangular refractive index profiles," J. Lightwave Technol. **25**, 1190–1197 (2007).
6. G. D. VanWiggeren, T. K. Gaylord, D. D. Davis, E. Anemogiannis, B. D. Garrett, M. I. Braiwish, and E. N. Glytsis, "Axial rotation dependence of resonances in curved CO_2-laser-induced long-period fibre gratings," Electron. Lett. **36**, 1354–1355 (2000).
7. G. D. VanWiggeren, T. K. Gaylord, D. D. Davis, M. I. Braiwish, E. N. Glytsis, and E. Anemogiannis, "Tuning, attenuating, and switching by controlled flexure of long-period fiber gratings," Opt. Lett. **26**, 61–63 (2001).
8. Y. P. Wang, Y. J. Rao, Z. L. Ran, T. Zhu, and A. Z. Hu, "A novel tunable gain equalizer based on a long-period fiber grating written by high-frequency CO_2 laser pulses," IEEE Photon. Technol. Lett. **15**, 251–253 (2003).
9. M. I. Braiwish, B. L. Bachim, and T. K. Gaylord, "Prototype CO_2 laser-induced long-period fiber grating variable optical attenuators and optical tunable filters," Appl. Opt. **43**, 1789–1793 (2004).
10. Y.-J. Rao, Y.-P. Wang, Z.-L. Ran, and T. Zhu, "Novel fiber-optic sensors based on long-period fiber gratings written by high-frequency CO_2 laser pulses," J. Lightwave Technol. **21**, 1320–1327 (2003).
11. Y. P. Wang, D. N. Wang, W. Jin, and Y. J. Rao, "Asymmetric transverse-load characteristics and polarization dependence of long-period fiber gratings written by a focused CO_2 laser," Appl. Opt. **46**, 3079–3086 (2007).
12. K. Brugger, "Effect of thermal stress on refractive index in clad fibers," Appl. Opt. **10**, 437–438 (1971).
13. G. W. Scherer, "Stress-induced index profile distortion in optical waveguides," Appl. Opt. **19**, 2000–2006 (1980).
14. Y. Hibino, F. Hanawa, and M. Horiguchi, "Drawing-induced residual stress effects on optical characteristics in pure-silica-core single-mode fibers," J. Appl. Phys. **65**, 30–34 (1989).
15. A. D. Yablon, "Optical and mechanical effects of frozen-in stresses and strains in optical fibers," IEEE J. Sel. Top. Quantum Electron. **10**, 300–311 (2004).
16. P. L. Chu and T. Whitbread, "Stress modification in optical fibre," Electron. Lett. **20**, 449–450 (1984).
17. P. C. P. Bouten, W. Hermann, C. M. G. Jochem, and D. U. Weichert, "Drawing influence on the lifetime of optical fibres," J. Lightwave Technol. **7**, 555–559 (1989).
18. S. M. Oh, P. H. Predieux, and X. G. Glavas, "Increased durability of optical fiber through the use of compressive cladding," Opt. Lett. **7**, 241–243 (1982).
19. D. I. Yeom, H. S. Kim, M. S. Kang, H. S. Park, and B. Y. Kim, "Narrow-bandwidth all-fiber acoustooptic tunable filter with low polarization-sensitivity," IEEE Photon. Technol. Lett. **17**, 2646–2648 (2005).
20. Y. Park, U.-C. Paek, and D. Y. Kim, "Determination of stress-induced intrinsic birefringence in a single-mode fiber by measurement of the two-dimensional stress profile," Opt. Lett. **27**, 1291–1293 (2002).
21. M. Ferrario, S. M. Pietralunga, M. Torregiani, and M. Martinelli, "Modification of local stress-induced birefringence in low-PMD spun fibers evaluated by high-resolution optical tomography," IEEE Photon. Technol. Lett. **16**, 2634–2636 (2004).
22. S. M. Pietralunga, M. Ferrario, M. Tacca, and M. Martinelli, "Local birefringence in unidirectionally spun fibers," J. Lightwave Technol. **24**, 4030–4038 (2006).
23. Y. Park, U.-C. Paek, and D. Y. Kim, "Complete determination of the stress tensor of a polarization-maintaining fiber by photoelastic tomography," Opt. Lett. **27**, 1217–1219 (2002).
24. I. H. Shin, B. H. Kim, S. P. Veetil, W. T. Han, and D. Y. Kim, "Residual stress relaxation in cleaved fibers," Opt. Commun. **281**, 75–79 (2008).
25. P. Y. Fonjallaz, H. G. Limberger, R. P. Salathe, F. Cochet, and B. Leuenberger, "Tension increase correlated to refractive-index change in fibers containing UV-written Bragg gratings," Opt. Lett. **20**, 1346–1348 (1995).
26. H. G. Limberger, C. Ban, R. P. Salathe, S. A. Slattery, and D. N. Nikogosyan, "Absence of UV-induced stress in Bragg gratings recorded by high-intensity 264 nm laser pulses in a hydrogenated standard telecom fiber," Opt. Express **15**, 5610–5615 (2007).
27. N. Belhadj, Y. Park, S. LaRochelle, K. Dossou, and J. Azana, "UV-induced modification of stress distribution in optical fibers and its contribution to Bragg grating birefringence," Opt. Express **16**, 8727–8741 (2008).
28. B. H. Kim, Y. Park, T. J. Ahn, D. Y. Kim, B. H. Lee, Y. Chung, U. C. Paek, and W. T. Han, "Residual stress relaxation in the core of optical fiber by CO_2 laser irradiation," Opt. Lett. **26**, 1657–1659 (2001).
29. B. H. Kim, T. J. Ahn, D. Y. Kim, B. H. Lee, Y. Chung, U. C. Paek, and W. T. Han, "Effect of CO_2 laser irradiation on the refractive-index change in optical fibers," Appl. Opt. **41**, 3809–3815 (2002).
30. H. S. Ryu, Y. Park, S. T. Oh, Y. J. Chung, and D. Y. Kim, "Effect of asymmetric stress relaxation on the polarization-dependent transmission characteristics of a CO_2 laser-written long-period fiber grating," Opt. Lett. **28**, 155–157 (2003).
31. F. Durr, H. G. Limberger, R. P. Salathe, F. Hindle, M. Douay, E. Fertein, and C. Przygodzki, "Tomographic measurement of femtosecond-laser induced stress changes in optical fibers," Appl. Phys. Lett. **84**, 4983–4985 (2004).
32. F. Durr, G. Rego, P. V. S. Marques, S. L. Semjonov, E. M. Dianov, H. G. Limberger, and R. P. Salathe, "Tomographic stress profiling of arc-induced long-period fiber gratings," J. Lightwave Technol. **23**, 3947–3953 (2005).
33. A. D. Yablon, M. F. Yan, D. J. DiGiovanni, M. E. Lines, S. L. Jones, D. N. Ridgway, G. A. Sandels, I. A. White, P. Wisk, F. V.

DiMarcello, E. M. Monberg, and J. Jasapara, "Frozen-in viscoelasticity for novel beam expanders and high-power connectors," J. Lightwave Technol. **22**, 16–23 (2004).
34. B. L. Bachim and T. K. Gaylord, "Microinterferometric optical phase tomography measuring small, asymmetric refractive-index differences in the profiles of optical fibers and fiber devices," Appl. Opt. **44**, 316–327 (2005).
35. B. L. Bachim, T. K. Gaylord, and S. C. Mettler, "Refractive-index profiling of azimuthally asymmetric optical fibers by microinterferometric optical phase tomography," Opt. Lett. **30**, 1126–1128 (2005).
36. M. Sochacka, "Optical fibers profiling by phase-stepping transverse interferometry," J. Lightwave Technol. **12**, 19–23 (1994).
37. A. D. Yablon, "Multi-wavelength optical fiber refractive index profiling by spatially resolved Fourier transform spectroscopy," J. Lightwave Technol. **28**, 360–364 (2010).
38. T. Colomb, F. Durr, E. Cuche, P. Marquet, H. G. Limberger, R. P. Salathe, and C. Depeursinge, "Polarization microscopy by use of digital holography: Application to optical-fiber birefringence measurements," Appl. Opt. **44**, 4461–4469 (2005).
39. L. Bruno, L. Pagnotta, and A. Poggialini, "A full-field method for measuring residual stresses in optical fiber," Opt. Lasers Eng. **44**, 577–588 (2006).
40. P. Kniazewski, T. Kozacki, and M. Kujawinska, "Inspection of axial stress and refractive index distribution in polarization-maintaining fiber with tomographic methods," Opt. Lasers Eng. **47**, 259–263 (2009).
41. B. Sevigny, F. Busque, N. Godbout, S. Lacroix, and M. Faucher, "High-resolution refractive index anisotropy measurement in optical fibers through phase retardation modulation," Appl. Opt. **47**, 1215–1222 (2008).
42. A. Barty, K. A. Nugent, D. Paganin, and A. Roberts, "Quantitative optical phase microscopy," Opt. Lett. **23**, 817–819 (1998).
43. M. R. Teague, "Deterministic phase retrieval: a Green's function solution," J. Opt. Soc. Am. **73**, 1434–1441 (1983).
44. A. Barty, K. A. Nugent, A. Roberts, and D. Paganin, "Quantitative phase tomography," Opt. Commun. **175**, 329–336 (2000).
45. N. M. Dragomir, G. W. Baxter, and A. Roberts, "Phase-sensitive imaging techniques applied to optical fibre characterisation," IEE Proc. Optoelectron. **153**, 217–221 (2006).
46. N. M. Dragomir, X. M. Goh, C. L. Curl, L. M. D. Delbridge, and A. Roberts, "Quantitative polarized phase microscopy for birefringence imaging," Opt. Express **15**, 17690–17698 (2007).
47. M. R. Hutsel, R. R. Ingle, and T. K. Gaylord, "Accurate cross-sectional stress profiling of optical fibers," Appl. Opt. **48**, 4985–4995 (2009).
48. M. R. Hutsel, R. R. Ingle, and T. K. Gaylord, "Technique and apparatus for accurate cross-sectional stress profiling of optical fibers," IEEE Trans. Instrum. Meas. **60**, 971–979 (2011).
49. X. M. Goh, N. M. Dragomir, D. N. Jamieson, A. Roberts, and D. X. Belton, "Optical tomographic reconstruction of ion beam induced refractive index changes in silica," Appl. Phys. Lett. **91**, 181102 (2007).
50. E. Ampem-Lassen, F. Sidiroglou, J. L. Peng, S. T. Huntington, and A. Roberts, "Index mapping for fibers with symmetric and asymmetric refractive index profiles," Opt. Express **16**, 10912–10917 (2008).
51. N. M. Dragomir, X. M. Goh, and A. Roberts, "Three-dimensional refractive index reconstruction with quantitative phase tomography," Microsc. Res. Tech. **71**, 5–10 (2008).
52. J. Hsieh, *Computed Tomography: Principles, Design, Artifacts, and Recent Advances* (SPIE Press, 2003).
53. A. Barty, "Quantitative phase-amplitude microscopy," Ph.D. thesis (University of Melbourne, Parkville, 2000).
54. D. Paganin, A. Barty, P. J. McMahon, and K. A. Nugent, "Quantitative phase-amplitude microscopy. III. The effects of noise," J. Microsc. **214**, 51–61 (2004).
55. A. Roberts, E. Ampem-Lassen, A. Barty, K. A. Nugent, G. W. Baxter, N. M. Dragomir, and S. T. Huntington, "Refractive-index profiling of optical fibers with axial symmetry by use of quantitative phase microscopy," Opt. Lett. **27**, 2061–2063 (2002).
56. M. R. Hutsel, C. C. Montarou, A. I. Dachevski, and T. K. Gaylord, "Algorithm performance in the determination of the refractive-index profile of optical fibers," Appl. Opt. **47**, 760–767 (2008).
57. F. Mitschke, *Fiber Optics: Physics and Technology* (Springer, 2009).
58. A. D. Yablon, M. F. Yan, P. Wisk, F. V. DiMarcello, J. W. Fleming, W. A. Reed, E. M. Monberg, D. J. DiGiovanni, J. Jasapara, and M. E. Lines, "Refractive index perturbations in optical fibers resulting from frozen-in viscoelasticity," Appl. Phys. Lett. **84**, 19–21 (2004).
59. Y. Park, U.-C. Paek, S. Han, B.-H. Kim, C.-S. Kim, and D. Y. Kim, "Inelastic frozen-in stress in optical fibers," Opt. Commun. **242**, 431–436 (2004).
60. F. Durr, H. G. Limberger, R. P. Salathe, and A. D. Yablon, "Inelastic strain birefringence in optical fibers," in *Optical Fiber Communication Conference* (Optical Society of America, 2006).
61. M. R. Hutsel and T. K. Gaylord, School of Electrical and Computer Engineering, Georgia Institute of Technology, Atlanta, GA 30332, USA, are preparing a manuscript to be called "Residual stress relaxation and densification in CO_2-laser-induced long-period fiber gratings."
62. D. A. Viskoe and G. W. Donohoe, "Optimal computed tomography data acquisition techniques and filter selection for detection of small density variations," IEEE Trans. Instrum. Meas. **45**, 70–76 (1996).